Microstructural creep, fatigue and creep-fatigue modeling of Nickel-based superalloy Inconel 617 at high temperature

Xiang Zhang, Tung Van Phan, Caglar Oskayy

Civil and Environmental Engineering Department, Vanderbilt University, Nashville, TN, USA 37235
xiang.zhang@vanderbilt.edu

ABSTRACT

Inconel 617 is a solution strengthened nickel-based alloy which has been considered as one of the leading structural material for the intermediate heat exchangers (IHX) in very high temperature reactor (VHTR). In order to gain understanding of the creep and fatigue deformation mechanisms and their interactions in alloy 617 operating in the VHTR environment, a computational model that operates at the microstructural scale has been developed for creep, fatigue and creep-fatigue modeling of alloy 617. This model is based on an isothermal, large deformation crystal plasticity finite element (CPFE) formulation and idealizes the deformation in the crystal lattice as collective glide and climb of dislocations. A recently developed glide resistance evolution equation by the authors that can capture the intermediate softening observed in both fatigue and creep-fatigue cycles of Inconel 617 at high temperature is adopted for the dislocation glide formulation. Dislocation climb is incorporated to account for the interactions between dislocations and local point defects at high temperature. The CP equations are solved incrementally as the constitutive relationship in the context of FE analysis on fully resolved microstructure reconstructed from experiment data. Model parameters are calibrated and verified using experimental tests.

I. INTRODUCTION

Nickel based alloy Inconel 617 is considered as a primary candidate structural material for the intermediate heat exchangers ([1]) in the VHTR applications. VHTR operating environment poses a challenge for structural materials due to requirements for very high temperature (up to 950 °C) strength as well as high temperature creep and damage resistance due to the long term in-service time and operation startup and shutdown cycles. Prediction of failure and life of this alloy under high temperature fatigue and creep-fatigue conditions is therefore a critical concern. Developing a computational model that incorporates the underlying physics of the plastic deformation, which can lead to the ability to capture the response in cyclic loading, and ultimately, life prediction capability draws significant research interest.

Extensive experimental studies have been conducted to study the high temperature response of Alloy 617 under different loading conditions, including temperature and strain rate dependency ([2, 3]) under monotonic loading, fatigue and creep-fatigue response under cyclic loading conditions with different strain ranges and hold times ([4, 5, 6, 7]) and long term creep response ([8]). Microstructure examinations showed failure is controlled by intergranular fracture under creep-fatigue loading, while transgranular cracking dominates when subjected to pure fatigue loads [6].

Crystal plasticity finite element method (CPFE) has been a well-established method that is capable of relating the microstructural heterogeneities and their interactions to the macroscale response (see a detailed review in Ref. [9]). CPFE used to model the fatigue and creep-fatigue response of Inconel 617 has been very recently [10]. It has been pointed out that while dislocation glide is the main deformation mechanism at lower temperature (i.e., below 0.5 T_M with T_M being the melting point) for metals, dislocation climb resulting from the interaction between dislocation and local non-equilibrium concentrations of point defects also take place at high temperature [11].

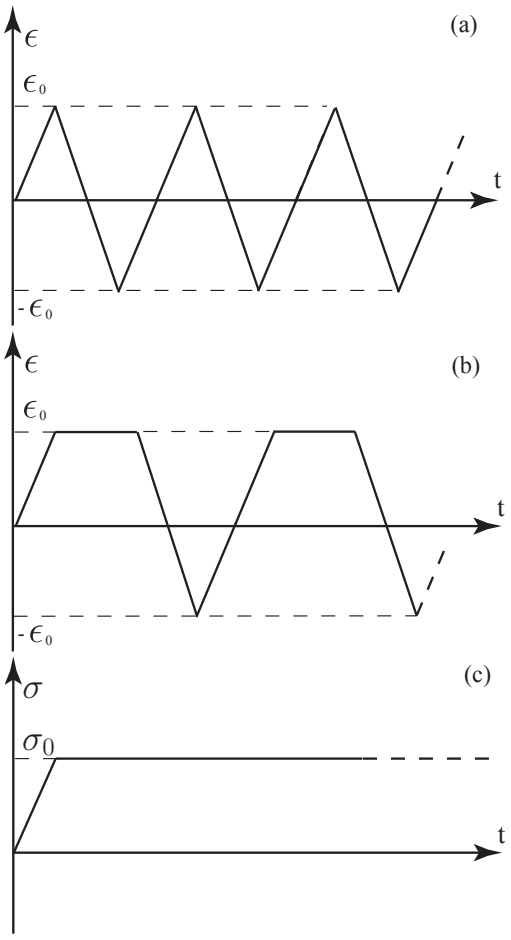

Fig. 1. Loading profiles: (a) strain controlled fatigue test; (b) strain controlled creep-fatigue test; (c) creep test.

In this manuscript, a crystal plasticity model considering dislocation glide and climb to idealize the creep-fatigue cycles of Inconel 617 at high temperature is developed. The fatigue and creep-fatigue loadings to mimic the operation cycles of VTHR and the creep loadings for evaluating their long term in-service performance (loading profile schematically shown in

Figure (1)) are of our primary research interest in the current study. The CPFE model consider large deformation kinematics and incorporates a new glide resistance evolution equation that can capture the above mentioned softening caused by the solute-drag creep effects, while dislocation climb is incorporated to accurately capture the creep strain.

II. MODEL DEVELOPMENT

Crystal plasticity finite element analysis of a single crystal was first carried out by Peirce, Asaro and Needleman [12, 13]. CPFEM has its advantage of flexible incorporation of available deformation mechanism and accounts for full microstructure heterogeneity and their interactions, hence is widely used for modeling the response of metallic materials under different loading conditions [14] across different deformation mechanisms [15, 16, 11, 17].

II.A. Kinematics of Crystal Plasticity

For a crystalline solid subjected to deformation gradient $\mathbf{F}$, it has been a standard procedure to decompose the deformation gradient into deformation and rotations to facilitate the constitutive description. While there are are two different decompositions of $\mathbf{F}$ available in literature [18, 19] depending on one or two intermediated configurations considered, our current formulation adopts the two intermediate configurations following Marin and Dawson [20]. This formulation has its kinematic theory originated from the work of Asaro [21], Tayler [21] and Hill and Rice [22]. This framework is briefly revisited here for completeness and clarity.

Consider the deformation gradient $\mathbf{F}$ that relates the current (deformed) configuration $\mathbb{B}$ with its reference (undeformed) configuration $\mathbb{B}_0$ of a polycrystalline solid, which can be multiplicatively decomposed into its elastic ($\mathbf{F}^e$) and plastic ($\mathbf{F}^p$) contributions as:

$$\mathbf{F} = \mathbf{F}^e \cdot \mathbf{F}^p \tag{1}$$

Further polar decomposition of the elastic part gives:

$$\mathbf{F} = \mathbf{V}^e \cdot \mathbf{F}^*, \qquad \mathbf{F}^* = \mathbf{R}^e \cdot \mathbf{F}^p \tag{2}$$

in which, $\mathbf{V}^e$ are the elastic stretch tensor and $\mathbf{R}^e$ the orthogonal rotation tensor. This decomposition introduces two intermediate configurations between $\mathbb{B}_0$ and $\mathbb{B}$ (see [20, 10] for details), and current formulation is written in the intermediate configuration $\widetilde{\mathbb{B}}$ obtained by unloading the deformed configuration through the elastic stretch $\mathbf{V}^{e-1}$, where the lattice orientation is the same as that in the current configuration.

Lattice orientation in the reference configuration is characterized by two orthogonal unit normals, $\mathbf{m}_0$ and $\mathbf{n}_0$, perpendicular to the glide plane and along the glide direction respectively. Evolution of lattice orientation is from the rotation tensor $\mathbf{R}^e$ as:

$$\begin{aligned} \mathbf{n}^\alpha &= \tilde{\mathbf{n}}^\alpha = \mathbf{R}^e \cdot \mathbf{n}_0^\alpha \\ \mathbf{m}^\alpha &= \tilde{\mathbf{m}}^\alpha = \mathbf{R}^e \cdot \mathbf{m}_0^\alpha \end{aligned} \tag{3}$$

The velocity gradient in configuration $\widetilde{\mathbb{B}}$ is decomposed into the symmetric ($\widetilde{\mathbf{D}}^p$) and skew ($\widetilde{\mathbf{W}}^p$) parts as:

$$\widetilde{\mathbf{L}}^p = \widetilde{\mathbf{D}}^p + \widetilde{\mathbf{W}}^p \tag{4}$$

both of which have its contributions from dislocation glide (indicated by subscript g) and climb (indicated by subscript c) as:

$$\begin{aligned} \widetilde{\mathbf{D}}^p &= \widetilde{\mathbf{D}}^p_{\mathrm{g}} + \widetilde{\mathbf{D}}^p_{\mathrm{c}} \\ \widetilde{\mathbf{W}}^p &= \widetilde{\mathbf{W}}^p_{\mathrm{g}} + \widetilde{\mathbf{W}}^p_{\mathrm{c}} \end{aligned} \tag{5}$$

and the detailed expression of each term is provided below.

It is well recognized that elastic deformation is negligible compared to the plastic deformation for metals in general, we adopt the small elastic strain assumption [20, 23]:

$$\mathbf{V}^e = \mathbf{I} + \boldsymbol{\epsilon}^e, \quad \|\boldsymbol{\epsilon}^e\| \ll 1 \tag{6}$$

in which, $\boldsymbol{\epsilon}^e$ denotes elstic strains. Time differentiation and inverse operation is expressed as:

$$\dot{\mathbf{V}}^e = \dot{\boldsymbol{\epsilon}}^e, \;\; \mathbf{V}^{e-1} = \mathbf{I} - \boldsymbol{\epsilon}^e \tag{7}$$

in which, super script -1 indicates tensor inversion. This simplification will lead to the elastic stress-stress relationship as:

$$\boldsymbol{\tau} = \widetilde{\mathbb{C}} : \boldsymbol{\epsilon}^e; \;\; \boldsymbol{\tau} = \det(\mathbf{I} + \boldsymbol{\epsilon}^e)\boldsymbol{\sigma} \tag{8}$$

where, $\widetilde{\mathbb{C}}$ is the fourth order anisotropic crystal elasticity tensor, $\boldsymbol{\tau}$ the Kirchhoff stress.

Eqs. (1)-(8) provides the base of the the current formulation while detailed expression for the skew and symmetric parts of velocity gradient as a result of dislocation glide and climb are discussed in the following sections.

II.B. Dislocation Glide

Utilizing the small elastic strain assumption (Eqs. (6) and (7)), the symmetric and skew part of velocity gradient in configuration $\widetilde{\mathbb{B}}$ is derived as (see Ref. [23]):

$$\widetilde{\mathbf{D}}^p_g = \mathbf{R}^e \cdot \sum_{\alpha=1}^{N} \dot{\gamma}^\alpha_g (\mathbf{m}^\alpha_0 \otimes \mathbf{n}^\alpha_0)_S \cdot \mathbf{R}^{eT} = \sum_{\alpha=1}^{N} \dot{\gamma}^\alpha_g (\widetilde{\mathbf{Z}}^\alpha)_S \tag{9}$$

$$\widetilde{\mathbf{W}}^p_g = \widetilde{\boldsymbol{\Omega}}^e + \mathbf{R}^e \cdot \sum_{\alpha=1}^{N} \dot{\gamma}^\alpha_g (\mathbf{m}^\alpha_0 \otimes \mathbf{n}^\alpha_0)_A \cdot \mathbf{R}^{eT} = \widetilde{\boldsymbol{\Omega}}^e + \sum_{\alpha=1}^{N} \dot{\gamma}^\alpha_g (\widetilde{\mathbf{Z}}^\alpha)_A \tag{10}$$

where, the subscripts S and A indicate the symmetric and skew (anti-symmetry) components, respectively (i.e., $(\cdot)_S = ((\cdot) + (\cdot)^T)/2$; $(\cdot)_A = ((\cdot) - (\cdot)^T)/2$ with superscript T indicates tensor transpose). $\widetilde{\boldsymbol{\Omega}}^e = \dot{\mathbf{R}}^e \cdot \mathbf{R}^{eT}$ denotes the spin of the lattice in configuration $\widetilde{\mathbb{B}}$, and possesses skew symmetry [24]. $\widetilde{\mathbf{Z}}^\alpha = \tilde{\mathbf{m}}^\alpha \otimes \tilde{\mathbf{n}}^\alpha$ is the Schmid tensor that resolves the applied stress onto glide system α as resolved shear stress (RSS, denoted as τ^α_g, and $\tau^\alpha_g = \boldsymbol{\tau} : \widetilde{\mathbf{Z}}^\alpha$) to drive the accumulation of shear strain rate $\dot{\gamma}^\alpha_g$ on individual glide system as shown in Figure 2. $\dot{\gamma}^\alpha_g$ is generally characterized by the flow rule as a function of τ^α and a set of internal state variables.

Several flow rules have been developed in literature to model the kinematics of dislocation glide at high temperature

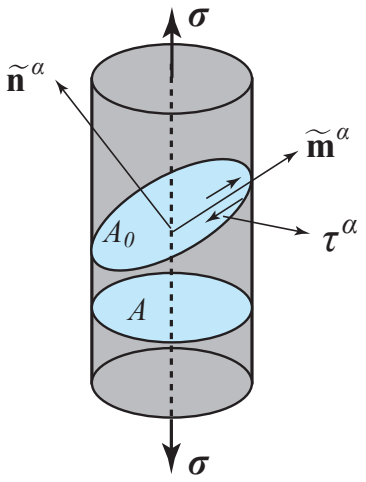

Fig. 2. Dislocation glide geometry.

([13, 25, 26, 27]) and we adopt the one developed by Busso [25, 28]:

$$\dot{\gamma}_g^{\alpha} = \dot{\gamma}_0 \exp\left\{ -\frac{F_0}{k\theta}\left\langle 1 - \left\langle \frac{|\tau^{\alpha} - B^{\alpha}| - S^{\alpha}\mu/\mu_0}{\hat{\tau}_0\mu/\mu_0} \right\rangle^{p} \right\rangle^{q} \right\} \mathrm{sgn}(\tau^{\alpha} - B^{\alpha}) \tag{11}$$

in which, k is the Boltzmann constant, θ the temperature in Kelvin, $\dot{\gamma}_0$ the reference shear strain rate, F_0 the activation energy. $\hat{\tau}_0$ the threshold stress at which dislocations can be mobilized without the assistance of thermal activation. p and q are two fitting parameters, μ and μ_0 the shear moduli at the current temperature and 0 K, respectively. S^{α} and B^{α} are two internal state variables: the glide resistance and backstress in the glide system α, respectively. sgn$(\cdot)$ is the sign function and $\langle\cdot\rangle$ denotes the Macaulay brackets (i.e., $< \cdot >= ((\cdot) + |\cdot|)/2)$.

The evolution equations for the backstress (S^{α}) is based on the work of Busso and Lin [28, 29], which is expressed as:

$$\dot{B}^{\alpha} = [h_B - D^{\alpha}B^{\alpha}\mathrm{sgn}(\dot{\gamma}^{\alpha})]\dot{\gamma}^{\alpha} \tag{12}$$

where, h_B and D^{α} are the hardening and dynamic recovery parameters for the backstress evolution, and D^{α} is expressed as [29]:

$$D^{\alpha} = \frac{h_B\mu_0}{S^{\alpha}}\left\{\frac{\mu_0'}{f} - \mu\right\}^{-1} \tag{13}$$

in which, μ_0' is the local slip shear modulus at 0 K and f is a parameter that accounts for the coupling between the internal glide variables as well as the statistical effects.

A new glide resistance evolution equation has been recently proposed by the authors to capture the initial softening in first cycle of both fatigue and creep-fatigue tests as well as its persistent re-emergence in every load reversal immediately after the strain hold in the creep-fatigue tests. An initial peak followed by an exponential decrease to a stable flow stress in Inconel 617 at high temperatures has been attributed to the solute-drag creep deformation mechanism [5]. Similar behavior has been observed in other alloys (e.g., class I and class A aluminum alloys) that exhibit solute-drag creep at elevated temperatures ([30, 31, 32]). This solute drag-creep effects is modeled by using the glide resistance equation from Ref. [10]:

$$\dot{S}^{\alpha} = [h_S - d_D(S^{\alpha} - \bar{S}^{\alpha})]|\dot{\gamma}^{\alpha}| - h_2(S^{\alpha} - S_0^{\alpha})H\left(\dot{\gamma}_{\mathrm{th}} - \sum_{\alpha=1}^{n}|\dot{\gamma}^{\alpha}|\right) \tag{14}$$

where, $\dot{\gamma}_{\mathrm{th}}$ is the threshold rate for static recovery, h_2 the rate of static recovery parameter, $\bar{S}^{\alpha}$ the steady state flow strength parameter. $H(\cdot)$ denotes the Heaviside function. The first part of the glide resistance evolution includes the steady state flow strength parameter, $\bar{S}^{\alpha}$, which is typically lower than the "initial" glide resistance, S_0^{α}. The second part of the glide resistance evolution accounts for the recovery of strain softening in the form of static recovery. In the present model, the recovery initiation is possible only when dislocation motion reduces significantly, which is a necessary condition to stop the drag process. This evolution equation essentially describes the competition between the first and second components under different glide magnitudes, leading the glide resistance varies between S_0^{α} and $\bar{S}^{\alpha}$.

II.C. Dislocation Climb

The contribution of dislocation climb follows a similar expression as dislocation glide ([11]):

$$\widetilde{\mathbf{D}}_c^{\mathrm{p}} = \mathbf{R}^e \cdot \sum_{\alpha=1}^{N}\dot{\gamma}_c^{\alpha}(\mathbf{m}_0^{\alpha} \otimes \boldsymbol{\chi}_0^{\alpha})_S \cdot \mathbf{R}^{eT} = \sum_{\alpha=1}^{N}\dot{\gamma}_c^{\alpha}(\widetilde{\mathbf{K}}^{\alpha})_{\mathrm{S}} \tag{15}$$

$$\widetilde{\mathbf{W}}_c^{\mathrm{p}} = \mathbf{R}^e \cdot \sum_{\alpha=1}^{N}\dot{\gamma}_c^{\alpha}(\mathbf{m}_0^{\alpha} \otimes \boldsymbol{\chi}_0^{\alpha})_A \cdot \mathbf{R}^{eT} = \sum_{\alpha=1}^{N}\dot{\gamma}_c^{\alpha}(\widetilde{\mathbf{K}}^{\alpha})_{\mathrm{A}} \tag{16}$$

in which, $\dot{\gamma}_c^{\alpha}$ is the shear strain rate as a result of dislocation climb. $\widetilde{\mathbf{K}}^{\alpha} = \widetilde{\mathbf{m}}^{\alpha} \otimes \widetilde{\boldsymbol{\chi}}$ is the climb tensor of climb system α in the crystal coordinate system ([33, 34]) with $\widetilde{\boldsymbol{\chi}}$ being the normal to the glide plane and parallel to the product of normal to the glide plane ($\tilde{\mathbf{n}}$) and the tangent to the dislocation line ($\tilde{\mathbf{t}}$) defined as ([33, 34]) :

$$\widetilde{\boldsymbol{\chi}} = \tilde{\mathbf{n}} \times \tilde{\mathbf{t}} \tag{17}$$

It is straight forward to see that the glide tensor depends on the glide system and this dependence is expressed in terms of a single parameter ψ (i.e., the angle between $\tilde{\mathbf{t}}$ and $\tilde{\mathbf{m}}$) as shown in Figure (3). The glide tensor is then expressed as:

$$\widetilde{\mathbf{K}}^{\alpha} = [\widetilde{\mathbf{m}} \otimes (\widetilde{\mathbf{m}} \times \widetilde{\mathbf{n}})]\cos\psi + (\widetilde{\mathbf{m}} \otimes \widetilde{\mathbf{m}})\sin\psi \tag{18}$$

Similar to the glide tensor, the climb tensor resolves the applied stress onto individual climb system (denoted as τ_c^{α}, and $\tau^{\alpha_c} = \boldsymbol{\tau} : \widetilde{\boldsymbol{K}}^{\alpha}$), and drives the shear strain to accumulate following a specific climb flow rule. The flow rule adopted here is based on the work of Lebensohn and coworkers ([34]) and takes into account the temperature and rate effects:

$$\dot{\gamma}_{\mathrm{c}}^{\alpha} = \dot{\gamma}_0 \exp\left(-\frac{F_0}{\kappa\theta}\right)\left(\frac{|\tau_{\mathrm{c}}^{\alpha}|}{\hat{\tau}_{0\mathrm{c}}}\right)^{p_{\mathrm{c}}} \mathrm{sgn}(\tau_{\mathrm{c}}^{\alpha}) \tag{19}$$

in which, $\dot{\gamma}_0$, F_0, κ and θ are the same parameters from the dislocation glide. $\hat{\tau}_{0c}$ is the threshold stress and p_c the creep exponent.

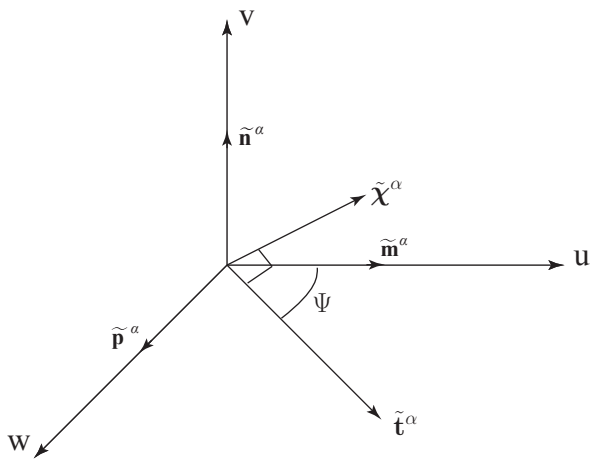

Fig. 3. Illustration of dislocation glide and climb systems: coordinate system $u-v-w$ is aligned with dislocation glide system α ($\tilde{\mathbf{p}}^{\alpha}$ is the unit vector to complete a right-hand orthogonal coordinate system defined by $\tilde{\mathbf{n}}^{\alpha}$ and $\tilde{\mathbf{m}}^{\alpha}$) and the clime system depends on the glide system through angle ψ.

III. MODEL PREPARATION AND CALIBRATION

III.A Experiments Employed

Strain-controlled low cycle fatigue and creep-fatigue tests were conducted by Wright and co-workeers [35] at constant strain rate of 1.0×10^{-3}/s and temperature of 950 °C using a symmetric triangular waveform (loading profile shown in Figure (1)). It need to be noted that during the first few cycles of most experiments, incrementally increasing strain values were used prior to reaching the target strain level to avoid overshooting the target strai. Table I summarizes the experiments used in this study. Creep tests at relative low hold stress (24.0 and 28.6 MPa) for alloy 617 at 950 reported by Wright and coworkers [8] were also employed in our current study.

All experimental data used in this study are from specimens machined from the annealed plate produced by ThyssenKrupp VDM and solution annealed at 1175 °C [35]. EBSD technique was used to examine the as-received specimen to determine the grains size statics and also texture which shows a bi-modal grain size distribution and random orientation [10].

III.B Microstructure Generation and Determination of Microstructure Size

Grain size distribution and orientation distribution information from the experimental EBSD study are used to construct the microstructure in software DREAM.3D ([36]). Two methods are available for the microstructure reconstruction in DREAM.3D. One is feeding a series of continuous EBSD scans along the thickness direction of the specimen into DREAM.3D reconstruct the exact microstructure. The second is providing directly the microstructure statics and morphological information to construction microstructure of user specified dimension processing the provided statics and morphological information. In this study, the bi-modal grain size distribution and random orientation from Ref. [10] are used to reconstruct the microstructure.

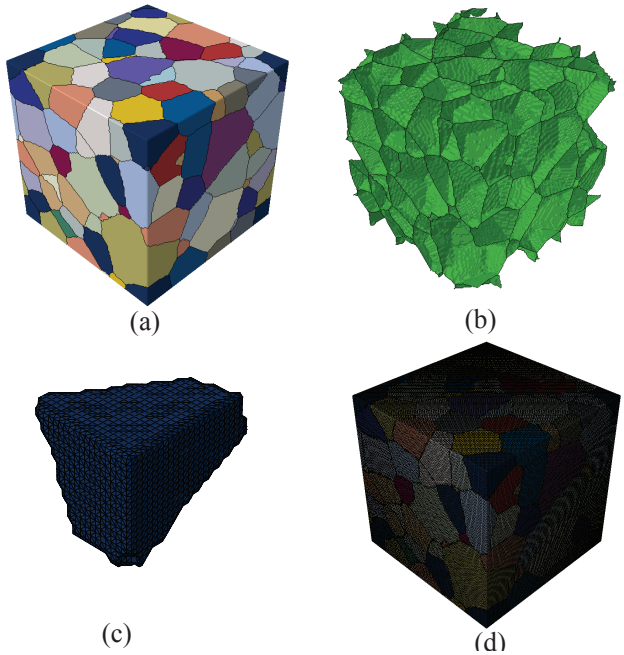

Fig. 4. Microstructure reconstruction and meshing: (a) Microstructure reconstruction in DREAM.3D; (b) Surface Mesh of individual Grains; (c) Volume mesh of individual grains using corresponding surface mesh; (4) Stitching grain mesh together to form polycrystal mesh.

Once the microstructure is reconstructed, surface mesh of each grain can be generated and exported from DREAM.3D, after which, the Parallelized Polycrystal Mesher (PPM) software developed by Cerrone et al [37] is used to generate volume mesh for individual grains and stitch them together to form the volume mesh of the whole microstructure. This microstructure reconstructions and meshing process is schematically demonstrated in Figure. 4.

In general, a microstructure need to be large enough be statistically representative. In order to choose the smallest representative volume element (RVE) to balance the computational efficiency and accuracy, a microstructure convergence study has been conducted using a creep-fatigue simulation. 140 grains have been identified to be appropriate for the current study and shows convergence in terms of both overall stress-strain response as well as local stress distribution [10]. This RVE mesh together with the boundary and loading conditions are shown in Figure 5. All numerical simulations are performed using this RVE.

III.B. Parameter Calibration

The parameters of dislocation glide have already been calibrated and discussed in Ref. [10]. Dislocation glide parameters hence are kept the same in the current study. Three dislocation climb parameters, p_c, ψ and $\hat{\tau}_{0c}$ need to be identified. Three tests, one from fatigue tests, one from creep-fatigue tests and one from the creep tests as highlighted in Table (I) are used for

Test name	Temperature(°C)	Strain rate s^{-1}	Strain range %	Hold time(s)	Hold stress MPa
B-14	950	0.001	0.6	0	NA
E-11	950	0.001	1.0	0	NA
J-1	950	0.001	1.0	0	NA
A-13	950	0.001	1.0	600	NA
B-16	950	0.001	0.6	180	NA
F-5	950	0.001	1.0	180	NA
C-2	950	NA	NA	NA	28.6
C-1	950	NA	NA	NA	24.0

TABLE I. Summary of experiments studied in current study.

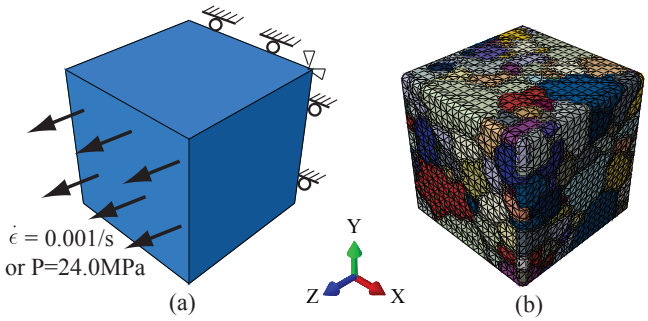

Fig. 5. Boundary conditions and Microstructure discretization.

the calibration purpose. For the fatigue and creep-fatigue tests, we are seeking to match the first cycle stress-strain response between simulation and experiments. For creep tests, the goal is to capture secondary creep.

Considering the small number of parameters need to be calibrated, the calibration process starts on a parametric study to investigate the sensitivity of each parameter followed by extensive simulations using Taylor hypothesis to quickly arrive at a set of parameter that provides acceptable match for the three tests used for calibration. The obtained parameters was further fine tuned by conduct CPFE simulations on the above mentioned 140-grain RVE. This calibration process yield the parameter sets $\psi = 60°$, $p_c = 2.95$ and $\hat{\tau}_{0c} = 1.05$MPa. The comparison between simulations and experimental tests of the three tests using the calibrated parameters are shown in Figure 6 and all the tests shows a reasonable match.

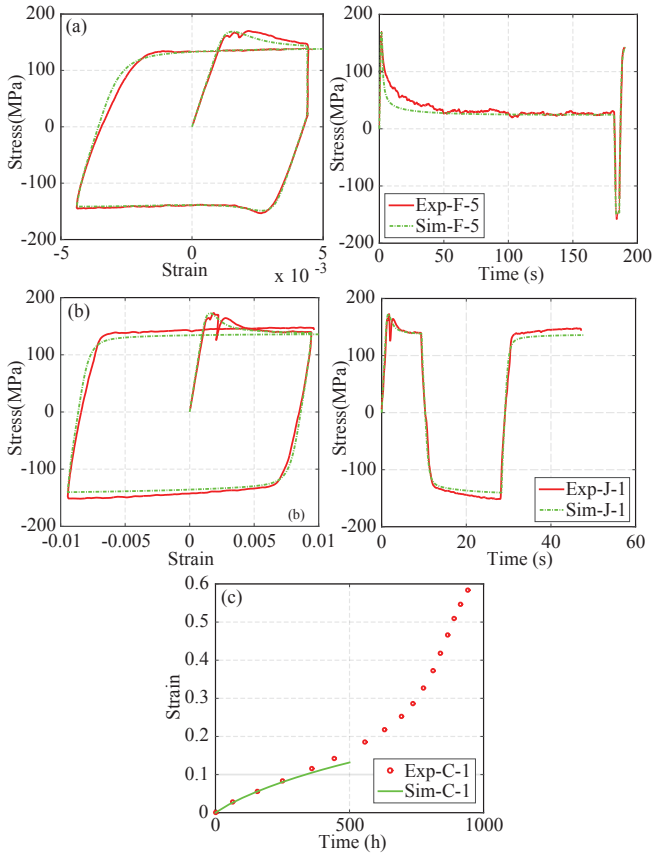

Fig. 6. Calibrated results: (a) creep-fatigue test F-5; (b) fatigue test J-1; (c) creep test C-1.

IV. MODEL VERIFICATION AND RESULTS ANALYSIS

The calibrated parameters are further validated by running CPFE simulations to compare the first cycle response of fatigue and creep-fatigue tests and secondary creep of creep-tests with experimental data using the remaining tests. As illustrated in Table I, the tests were performed using various strain ranges and hold times for fatigue and creep-fatigue tests and different hold stress for creep tests and the comparison are shown in Figure 7.

The transient stress relaxation phenomenon caused by solute-drag creep is most prominent in the first cycle, we mainly investigate the predictive capability of the proposed model in capturing the hysteresis behavior of the first cycle for fatigue and creep-fatigue tests. The initial tensile loading part of the stress-strain curves in all fatigue and creep experiments is also marked by the presence of serrations induced by the Portevin-Le Chatelier effect [5]. The current formulation does not account for this effect and the tensile loading part of the simulations exhibit a smooth loading path.

For the creep tests as shown in Figure 7 (c), the experiments shows a significant tertiary creep following the secondary creep. However our current formulation does not include any microstructural grain boundary damage effects to account for

the tertiary creep. The match is reasonable up to the onset of damage.

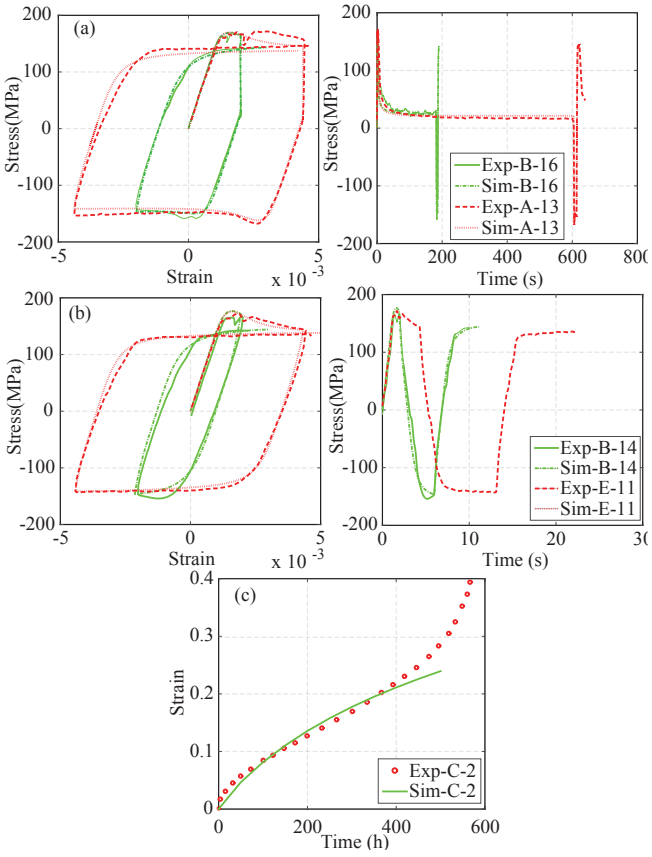

Fig. 7. Verification results: (a) Creep test B-16 and A-13; (b) fatigue text B-14 and E-11; (c) creep test C-2.

In view of the above-mentioned points, the simulated overall stress-strain hysteresis curves are in very good agreement with the experiments. In particular, the stress relaxations caused by solute-drag creep are accurately captured as a function of various hold times and strain ranges.

CONCLUSIONS AND FUTURE STUDY

A CPFE model considering both dislocation glide and climb has been developed to model the creep, fatigue and creep-fatigue response of Inconel 617 at high temperature. The model adopts a glide resistance evolution that consider the solute-drag creep effects to capture the softening observed in the fatigue and creep-fatigue tests and also incorporates the climb mechanism to capture the creep strain at low hold stress (compared with the yield stress) in the creep tests. Verification of the model points to a good match between simulation and experiments in terms of stress-strain and stress-time response in fatigue and creep-fatigue tests as well as secondary creep in creep tests.

The current model assumes full traction continuity along grain boundaries and did not incorporate any damage effects. Future work will consider cohesive zone modeling of the grain boundaries, which will allow the crack initialization prediction at grain boundaries to capture the cyclic softening in fatigue and creep-fatigue tests as well as tertiary creep in creep tests up until failure. On the other hand, to gain the capability for structural scale analysis, the proposed model will be coupled to structural scale simulations either through concurrent-hierarchical multiscale modeling (e.g., [38, 39, 40]), or through sequential multiscale modeling to calibrate model parameters of phenomenological models (e.g., [41, 42]).

ACKNOWLEDGMENTS

The authors gratefully acknowledge the research funding from the US Department of Energy, Nuclear Energy University Program (Grant No: 62-0476822). We acknowledge the technical cooperation with Prof. Yongming Liu at Arizona State University for providing experimental EBSD data for Inconel 617, and Dr. Richard Wright at Idaho National Laboratory for providing experimental fatigue and creep fatigue data.

REFERENCES

1. Y. SHI, K. YUAN, X. ZHAO, and Y. WU, "Study on Comparison Between Inconel 617 and Gh3128 as Structural Material Candidates for Intermediate Heat Exchanger," in "Proceedings of the 2013 21st International Conference on Nuclear Engineering ICONE21," ASME (2013).
2. W. REN and R. W. SWINDEMAN, "A Review on Current Status of Alloys 617 and 230 for Gen IV Nuclear Reactor Internals and Heat Exchangers," *ASME. J. Pressure Vessel Technol.*, **131** (2009).
3. J. WRIGHT, J. SIMPSON, R. WRIGHT, L. CARROLL, and T. SHAM, "STRAIN RATE SENSITIVITY OF ALLOYS 800H AND 617," in "Proceedings of the 2013 ASME Pressure Vessels & Piping Conference," Paris, France (2013).
4. X. CHEN, M. A. SOKOLOV, S. SHAM, D. L. E. III, J. T. BUSBY, K. MO, and J. F. STUBBINS, "Experimental and modeling results of creep-fatigue life of Inconel 617 and Haynes 230 at 850 °C," *J. Nucl. Mater.*, **432**, 94–101 (2013).
5. J. K. WRIGHT, L. J. CARROLL, J. A. SIMPSON, and R. N. WRIGHT, "Low Cycle Fatigue of Alloy 617 at 850°C and 950°C," *J. Eng. Mater. Technol.*, **135**, 031005 (2013).
6. L. CARROLLA, C. CABETB, M. CARROLLA, and R. WRIGHT, "The development of microstructural damage during high temperature creepfatigue of a nickel alloy," *Int. J. Fatigue*, **47**, 115–125 (2013).
7. J. K. WRIGHT, L. J. CARROLL, C. CABET, T. M. LILLO, J. BENZ, J. A. SIMPSON, W. R. LLOYD, J. A. CHAPMAN, and R. N. WRIGHT, "Characterization of elevated temperature properties of heat exchanger and steam generator alloys," *Nucl. Eng. Des.*, **251**, 252–260 (2012).
8. R. W. J. K. WRIGHT, L. J. CARROLL, "Creep and Creep-Fatigue of Alloy 617 Weldments," Tech. rep., Idaho National Laboratory (2014).
9. F. ROTERS, P. EISENLOHR, L. HANTCHERLI, D. TJAHJANTO, T. BIELER, and D. RAABE, "Overview of constitutive laws, kinematics, homogenization and multiscale methods in crystal plasticity finite-element modeling:

Theory, experiments, applications," *Acta Mater.*, **58**, 1152–1211 (2010).
10. X. ZHANG and C. OSKAY, "Polycrystal plasticity modeling of nickel-based superalloy IN 617 subjected to cyclic loading at high temperature," *Modelling Simul. Mater. Sci. Eng.*, **24**, 055009 (2016).
11. R. A. LEBENSOHN, C. S. HARTLEY, C. N. TOMÃL', and O. CASTELNAU, "Modeling the mechanical response of polycrystals deforming by climb and glide," *Phil. Mag. A*, **90**, 5, 567–583 (2010).
12. D. PEIRCE, R. ASARO, and A. NEEDLEMAN, "An analysis of nonuniform and localized deformation in ductile single crystals," *Acta Metall.*, **30**, 1087–1119 (1982).
13. D. PEIRCE, R. ASARO, and A. NEEDLEMAN, "Material rate dependence and localized deformation in crystalline solids," *Acta Metall.*, **31**, 1951–1976 (1983).
14. T. SUGUI, X. JUN, Z. XIAOMING, Q. BENJIANG, L. JIANWEI, Y. LILI, and W. WUXIANG, "Microstructure and creep behavior of FGH95 nickel-base superalloy," *Mater. Sci. A*, **528**, 4-5, 2076–2084 (2011).
15. L. A. A. STAROSELSKY, "Inelastic deformation of polycrystalline face centered cubic materials by slip and twinning," *J. Mech. Phys. Solids*, **46**, 671–696 (1998).
16. T. BIELER, P. EISENLOHR, F. ROTERS, D. KUMAR, D. MASON, M. CRIMP, and D. RAABE, "The role of heterogeneous deformation on damage nucleation at grain boundaries in single phase metals," *Int. J. Plast.*, **25**, 9, 1655 – 1683 (2009), exploring New Horizons of Metal Forming Research.
17. J. THOMAS, M. GROEBER, and S. GHOSH, "Image-based crystal plasticity FE framework for microstructure dependent properties of Ti-6Al-4V alloys," *Materials Science and Engineering: A*, **553**, 164–175 (2012).
18. R. ARASO, "Crystal Plasticity," *J. Appl. Mech.*, **50**, 921–934 (1983).
19. E. ONAT, "Representation of inelastic behaviour in the presence of anisotropy and finite deformations," in D. OWEN and B. WILSHIRE, editors, "Recent Advances in Creep and Fracture of Engineering Materials and Structures," Pineridge Press, pp. 231–264 (1978).
20. E. MARIN and P. DAWSON, "On modelling the elasto-viscoplastic response of metals using polycrystal plasticity," *Comput. Methods Appl. Mech. Engrg.*, **165**, 1–21 (1998).
21. G. TAYLOR, "Plastic Strain in Metals," *J. Inst. Met.*, **62**, 307–324 (1938).
22. R. HILL and J. RICE, "Constitutive analysis of elastic-plastic crystals at arbitrary strain," *J. Mech. Phys. Solids*, **20**, 401–413 (1972).
23. E. B. MARIN, "On the formulation of a crystal plasticity model," Tech. rep., Sandia National Laboratories (2006).
24. T. BELYTSCHKO, W. LIU, B. MORAN, and K. EIKHODARY, *Nonlinear Finite Elements for Continua and Structures*, John Wiley and Sons, New York, 2nd ed. (2014).
25. E. P. BUSSO and F. A. MCCLINTOCK, "A dislocation mechanics-based crystallographic model of a B2-type intermetallic alloy," *Int. J. Plast.*, **12**, 1–28 (1996).
26. M. SHENOY, A. GORDON, D. MCDOWELL, and R. NEU, "Thermomechanical Fatigue Behavior of a Directionally Solidified Ni-Base Superalloy," *J. Eng. Mater. Technol.*, **127**, 325–336 (2005).
27. A. MA and F. ROTERS, "A constitutive model for FCC single crystals based on dislocation densities and its application to uniaxial compression of aluminium single crystals," *Acta Mater.*, **52**, 3603–3612 (2004).
28. E. BUSSO, F. MEISSONNIER, and N. O'DOWD, "Gradient-dependent deformation of two-phase single crystals," *J. Mech. Phys. Solids*, **48**, 2333–2361 (2000).
29. B. LIN, L. ZHAO, J. TONG, and H. CHRIST, "Crystal plasticity modeling of cyclic deformation for a polycrystalline nickel-based superalloy at high temperature," *Mater. Sci. Eng. A*, **527**, 3581–3587 (2010).
30. O. SHERBY and P. BURKE, "Mechanical behavior of crystalline solids at elevated temperature," *Prog. Mater. Sci.*, **13**, 323–390 (1968).
31. E. TALEFF, W. GREEN, M.-A. KULAS, T. R. MCNELLEY, and P. KRAJEWSKI, "Analysis, representation, and prediction of creep transients in Class I alloys," *Mater. Sci. Eng. A*, **410-411**, 32–37 (2005).
32. R. CARMONA, Q. ZHU, C. SELLARS, and J. BEYNON, "Controlling mechanisms of deformation of AA5052 aluminium alloy at small strains under hot working conditions," *Mater. Sci. Eng. A*, **393**, 157–163 (2005).
33. C. S. HARTLEY, "A method for linking thermally activated dislocation mechanisms of yielding with continuum plasticity theory," *Phil. Mag.*, **83**, 31-34, 3783–3808 (2003).
34. R. A. LEBENSOHN, C. S. HARTLEY, C. N. TOME, and O. CASTELNAU, "Modeling the mechanical response of polycrystals deforming by climb and glide," *Philos. Mag.*, **90**, 567–583 (2010).
35. J. K. WRIGHT, N. J. LYBECK, and R. N. WRIGHT, "Tensile Properties of Alloy 617 Bar Stock," Technical report, Idaho National Laboratory (2013).
36. M. GROEBER and M. JACKSON, "DREAM.3D: A Digital Representation Environment for the Analysis of Microstructure in 3D," *Integr. Mater. Manuf. Innov.*, **3**, 5–19 (2014).
37. A. CERRONE, J. TUCKER, C. STEIN, A. ROLLETT, and A. INGRAFFEA, "MICROMECHANICAL MODELING OF RENE88DT:FROM CHARACTERIZATION TO SIMULATION," in "Proceedings of the 2012 Joint Conference of the Engineering Mechanics Institute and the 11th ASCE Joint Specialty Conference on Probabilistic Mechanics and Structural Reliability," (2012).
38. C. OSKAY, "Variational multiscale enrichment for modeling coupled mechano-diffusion problems," *Int. J. Numer. Methods Eng.*, **89**, 6, 686–705 (2012).
39. X. ZHANG and C. OSKAY, "Eigenstrain based reduced order homogenization for polycrystalline materials," *Comput. Methods Appl. Mech. Engg.*, **297**, 408–436 (2015).
40. S. ZHANG and C. OSKAY, "Reduced order variational multiscale enrichment method for elasto-viscoplastic problems," *Comput. Methods Appl. Mech. Engg.*, **300**, 199–224 (2016).
41. C. OSKAY and M. HANEY, "Computational modeling of titanium structures subjected to thermo-chemo-mechanical environment," *Int. J. Solids Struct.*, **47**, 24, 3341–3351 (2010).

42. H. YAN and C. OSKAY, “A viscoelasticâĂŞviscoplastic model of titanium structures subjected to thermo-chemo-mechanical environment,” *Int. J. Solids Struct.*, **56âĂŞ57**, 29–42 (2015).